SLAC-PUB-7683
October, 1997

SOFT X-RAY PRODUCTION IN SPARK DISCHARGES IN HYDROGEN, NITROGEN, AIR, ARGON AND XENON GASES.

J. Va'vra
Stanford Linear Accelerator Center, Stanford University,
Stanford, CA 94309, U.S.A.

J. A. Maly
Applied Science Consultants
5819 Ettersberg Dr., San Jose, CA 95123, U.S.A.

P.M. Va'vra
67 Pine Lane, Los Altos, CA 94022, U.S.A.

ABSTRACT

We describe a generator of soft X-rays of energy between 2 and 10 keV by sparking in hydrogen, air, nitrogen, argon and xenon gases at low pressure with a sparking voltage as low as ~0.8 kV, which can be used as a simple monitor of the gaseous detectors. The X-ray production mechanism is discussed, including the possibility of a new process.

Submitted to Nuclear Instruments and Methods

The work was supported in part by Department of Energy contract DE-AC03-76SF00515.

1. INTRODUCTION

We present a simple X-ray generator which can be used to monitor drift chambers. The generator uses a spark gap operating at low pressure, with a thin window and very low voltages between 0.8 and 2.5 kV to create X-rays between 2 and 10 keV.

To create the X-rays by sparking in low pressure is not new. Less known is the fact that one can create the X-ray energies, which are larger than the sparking voltage. This seemingly surprising effect is semi-qualitatively explained in literature by so called "pinch" effect, which is known to occur during very large low inductance sparks, operating typically with initial charging voltages 10-60kV, charging capacitance 10-20μF, low inductance ~100 nH, stored energies 1-3 kJ/pulse and peak spark currents 100-200kA [1]. The pinch effect has been demonstrated experimentally using pin hole photography, which indicates a formation of point-like (plasma points) regions within the plasma [2]. A generally accepted explanation of the pinch effect is based on the radiation collapse model [1]. During the pinch effect, one observes a formation of dips in spark current, which in turn creates large local voltages [1]. The voltage across the sparking gap can exceed the supply voltage by a factor 2-3 [3], and thus the X-ray energies can exceed the sparking voltage. The current dips are correlated with the appearance of plasma points, which principally emit X-ray lines of the anode material; radiation from the cathode material is weak [1]. The X-ray production shows a strong angular anisotropy [4]. The sparks in the above tests are so large that the electrodes wear out quickly. Indeed, the spectral investigations reveal emission from heavily ionized atoms present in the electrode material [2].

In our tests, we tried to set the smallest possible sparks still consistent with the X-ray production, i.e. we tried to operate at opposite end of the spark stored energies mentioned above. The sparking voltage was varied between 0.8 and 2.1kV, the charging capacitance 75nF, inductance ~1000nH, stored energy 0.024-0.17J/pulse, the peak spark currents 0.2-0.5kA and the total spark charge between $4x10^{14}$ and 10^{15} electrons/spark. The observed X-ray energies were between 2 and 10 keV even at the lowest sparking voltage of ~0.8kV (depending on the gas), and following an exponential distribution falling towards larger X-ray energies. The maximum observed X-ray energy (~10keV), generated at the lowest voltage (~0.8kV), is above K-shell energy of typical gases we used in our tests, and materials used in our spark electrodes (see Table 1 and chapter 4). The X-ray production persists even for the carbon electrodes which have the smallest K-shell energy (0.284keV); this would appear to eliminate a theory that the electrode atoms are responsible for the X-ray production. Furthermore, we have evidence that the production threshold and the X-ray rate are dependent on the gas choice in the sparking vessel. We have measured the I(t), V(t) and dI/dt(t) curves and confirm that the X-rays are produced during the largest swing in the dI/dt(t) curve corresponding to a dip in the current I(t). This would appear to

be consistent with the earlier mentioned pinch effect mechanism. The sparks in our tests are relatively large by a typical standard, however, compared to the spark energies used in Ref.1-4, they are considerably smaller, by at least a factor of ~$4x10^4$ (at ~0.8kV). If we really observe the pinch effect it is occurring at the smallest spark energy reported so far in the literature, and we would then be investigating its threshold behavior.

However, we have some doubts that the pinch effect is really understood quantitatively. The sparking phenomenon is an extremely complex process if we insist on a real quantitative evaluation of its dynamics. Its understanding is not yet at a level of that of the electron transport at low drift electric fields or small avalanches, which can be solved reasonably accurately using the Monte Carlo simulation [5] (computer program follows the electrons and ions in small steps (fraction of a ps) and evaluates electrostatic forces, position and velocities of each electron and ion, and probability of various physics processes using the electron-molecule scattering cross-sections). It is not possible to do this for sparks having more than ~10^{15} electrons at this time not only because of the computational difficulties but also because one does not necessarily know details of all physics processes involved. For example, in chapter 4 we mention one additional possible mechanism which may have been neglected in the theory of pinch effect, and may contribute to the X-ray production in our tests.

One practical benefit of running small spark energy is that the sparking electrodes do not wear out quickly and the device is suited for long term investigations. The spark electromagnetic noise requires a careful shielding for fast detectors. For drift chambers with a long drift one can be easily protected by a drift time delay of about 1-2 μs. The X-rays were monitored at 90° in respect to the spark axis during all tests in this paper. An initial approximate observation indicates that they may be isotropic, although this is yet to be confirmed by a larger test detecting X-rays over a larger solid angle.

2. EXPERIMENTAL SETUP

2.1. Description of X-ray producing apparatus

Fig.1 shows schematically the spark producing apparatus. It uses a car spark gap with a 1 mm gap between the points, which is placed in a small brass vessel equipped with a thin window to allow low energy X-rays to penetrate (in final tests we also used carbon electrodes in a specially prepared spark gap). The window opening is ~1.27 cm diameter and its material is either 12.7 μm stainless steel (sealed by a conducting epoxy), or 50 μm Mylar foil. The sparking vessel is connected to a vacuum pump from one side, and to a gas bottle from another side. The gas pressure is controlled by a small needle valve throttling a gas flow while pumping. The pressure is

monitored by a thermocouple gauge with accuracy of a few microns ($1\mu = 10^{-3}$ Torr). The pump was capable of reaching a pressure 10-20μ.

The operating parameters of the spark gap were tuned to maximize the X-ray production. It turns out that this occurs in a relatively narrow window of the parameter space. The spark gap operates at low pressure between 0.2 and 1Torr, depending on the gas choice. It operates as a relaxation oscillator with a charging resistor R = 80kΩ and a charging capacitor C = 75nF. Because of excessive heating, the charging resistor R is made with an equivalent circuit involving six pairs of ~27kΩ, 10W resistors; it is necessary to cool them by a small fan. The high voltage power supply, capable of delivering up to 40 mA DC current, operates at +2.5kVDC voltage. The sparking voltage V_{spark} varies between 0.8 and 2.1kV, which corresponds to a spark energy ($\frac{1}{2}CV_{spark}^2$) between 0.024 and 0.17J/pulse, and a spark charge (CV_{spark}) between $4x10^{14}$ and 10^{15} electrons/spark. The spark repetition period T is set typically between 5 and 20ms by the choice of gas pressure, which corresponds to sparking rates between 50 and 200Hz.

2.2. Spark voltage monitoring

First, we calibrated the power supply DC output with a precision voltage divider and a digital voltmeter. This resulted in a small ~0.6% correction. Second, we calibrated a spark voltage V_{spark} relative to a spark period T using a special voltage divider, shown in Fig.2a. To monitor varying voltage by a voltage divider, it is necessary to compensate resistors for their parasitic capacitance. This was done by measuring a parasitic capacitance of the 300MΩresistor in Fig.2a, and then empirically tuning the 80nF capacitor to minimize an undershoot in the monitored voltage of Fig.2b. The monitored voltage of Fig.2b was used to determine a correlation between the sparking voltage V_{spark} and a sparking period T of the oscillator. By measuring the sparking period T one can uniquely determine the sparking voltage V_{spark}, which is shown in Fig.2c. Finally, we have also used a calibrated spark gap[1] CG3-1.5 to calibrate V_{spark}. Its sparking voltage was measured to be 1.4kV, i.e. for $V_{spark} < 1.4$kV, the spark gap did not fire, above 1.4kV it would light up. This was a simple way to confirm that our calibration is correct, and that there is no fast transient exceeding V_{spark}.

The relaxation oscillator has the following feature: for a given spark gap distance d, gas pressure p and gas choice, the sparking voltage V_{spark} is determined according to Paschen's law, which says that V_{spark} is a function of pd. We operated in a region of the law where increasing the pressure reduces the sparking voltage, which in turn reduces the sparking period T.

During the experiment, we would typically monitor the sparking period, which is easy to measure, and use the calibration curve of Fig.2c to obtain the corresponding sparking voltage.

[1] Made by General Instrument Co., Chicago, Il 60645, U.S.A.

Depending on the choice of the gas pressure in a given gas, we would typically select the sparking voltage V_{spark} between 0.8 and 2.1kV during this experiment, while running the high voltage power supply always at a constant value of +2.5kV. We used the scope triggering circuit, described in Fig.1, to determine the sparking frequency T.

2.3. X-ray detectors

We have used four types of X-ray detectors during this test: a Geiger detector TBM-3S[2] , a single wire proportional tube detector, a long drift detector, and the YAP scintillator[3] coupled to the XP2230 photomultiplier[4] . A choice of four very different methods was motivated by the desire to eliminate any detection dependent systematic effects. The most prominent systematic effect was the spark noise generated by the spark gap located very close to the detector. To limit its influence, we have constructed a large copper mesh Faraday cage around the detector, the connecting cables were placed in the grounded copper pipes, and the spark gap vessel and its high voltage connection was well grounded. The signal detection in the wire tube detector and the YAP scintillator occurs during the largest spark noise, and therefore it was necessary to place them in the second local coaxial shield. The easiest task to eliminate the spark noise was with the long drift detector because in this particular geometry one can easily separate the spark noise from the X-ray signal by a choice of a suitable electric drift field. In all cases it was easy to verify that we indeed detect the X-rays by placing an absorber between the spark plug vessel and the detector window.

The Geiger detector TBM-3S is a commercially made battery operated detector equipped with a thin Mylar window of a 1.5 mg/cm^2 thickness and 5 cm diameter. It is filled with halogen gas.

Fig. 3 shows the geometry of the wire tube detector. The gold plated tungsten anode wire diameter is 38 μm. The aluminum tube has 10 mm i.d. with a 1 mm wall thickness. The tube has a 10 mm x 10 mm opening in the center, which is covered with a 30 μm thick aluminized Mylar foil. The foil is connected electrically to the tube wall with conducting epoxy and sealed with a DP-190 epoxy. The detector is operating with a 95% Ar+5% CH_4 gas mixture at 1 atm pressure. This choice was primarily motivated by its non-flammability.

Fig. 4 shows the geometry of the long drift wire detector. The drift cell is made of two sections: a drift region made of equally spaced stainless steel rings and a gain region containing 20 μm gold plated anode wires surrounded by a nickel plated cathode. The drift field is defined by the potentials V_1 and V_2. The resistor chain provides voltages to the individual stainless steel rings. The value of each resistor is 10MΩ. The drift region has a cylindrical shape with 2.5 cm i.d. and

---

[2] Made by Technical Associates, Canoga Park, CA91303, U.S.A.

[3] YAP stands for $YAlO_3$:Ce; density 5.37 g/cm^3, peak emission at 370nm, typically 3-4 p.e./keV.

[4] Made by Amperex, North American Philips Co.

12 cm long active volume. The entrance window into the long drift detector is made of ~13 μm thick aluminized Mylar foil. The gas gain is controlled by the cathode voltage V_c. All anode wires are connected together to a single amplifier. The detector is also operating with a 95% Ar+5% CH_4 gas mixture at 1 atm pressure. To be insensitive to a spark noise, we would typically choose a drift field of only ~8-10V/cm corresponding to allow a very low electron drift velocity of ~5 mm/μs. Typically, with this detector, the spark noise would appear only in the first 1-2 μs after the scope trigger, followed by a perfect noise-free period. We would observe events of interest between 3 and 25 μs after the scope trigger.

The YAP scintillator was a cube (1cm x 1cm x 1cm) coupled to a XP2230 PM tube with a UV coupling grease. A good light collection was ensured by covering the sides of the scintillator with Teflon tape; the light leak was stopped with two layers of black paper tape. The PM tube operated at very low voltage of -1.4kV because we used an amplifier with a large gain (~15mV/pC). The main reason to use this detector was to investigate the high energy end (tens of keV) of the pulse height spectrum where the gaseous detectors start loosing efficiency.

2.4. Electronics used in the test

The long drift detector was used to measure the multiplicity of the X-ray bursts. Its amplifier was a battery operated charge sensitive amplifier with a gain ~15mV/pC, a shaping time ~65ns and σ_{noise}~2000 e^-. This sensitivity is enough to be able to detect even single electrons arriving on the wire, assuming that the gas gain is in the range of 10^5. A conversion of a 3-10keV X-ray generates a much larger signal equivalent to several hundred electrons.

The wire tube detector measured the X-ray pulse height spectra using two methods: (a) peak sensing method using a LeCroy TRA100 amplifier with a gain ~50mV/pC and a shaping time ~20 μs together with either a digital oscilloscope (reading individual pulses manually), (b) charge sensing method using the battery operated amplifier (see above) with the pulse height analyzer LeCroy QVT 3001 in q-mode operating with an external 400ns long gate (the YAP scintillator detector was also using this method).

2.5. Expected X-ray attenuation factors and detection efficiency

Figures 5a,b show calculated attenuation curves for various materials and an expected detection efficiency for the tube and long drift wire detectors. The attenuation factor is defined in a usual way as $\eta(E) = N/N_o = \exp(L/L_o)$, where L is the X-ray path length and L_o is the attenuation length calculated from the absorption coefficient in a given material [6]. The X-ray detection efficiency, $\varepsilon(E)$, defined as a ratio of detected and produced number of X-rays, was calculated as follows:

$$\varepsilon(E) = \eta_{mylar}(E)\,\eta_{air}(E)\,\eta_{window}(E)\,(1-\eta_{gas}(E)) \qquad (1)$$

where η_{gas} is the attenuation in 95% Ar+5% CH_4 gas mixture, and other factors are the attenuation factors in the materials in the X-ray path. We assume that the wire chamber detection efficiency is close to 100% for a charge generated by the X-rays. From Fig. 5b one can see that the long drift detector has a good X-ray detection efficiency between 3 and 20keV.

3. EXPERIMENTAL RESULTS

We have observed X-ray production with all four types of detectors described in chapter 2.3. There are three arguments for this statement: (a) the radiation was not affected by a strong magnet placed between the sparking vessel and the detector, indicating that we are indeed dealing with the X-rays or neutral particles; (b) the range measurements are very consistent with the X-ray production; (c) the response from the gaseous detectors strongly indicates soft X-ray production (pulses are comparable in size and shape to pulses from an Fe^{55} X-ray source). The X-rays were monitored at 90° in respect to the spark axis during all tests in this paper.

3.1. Observation of X-ray showers

The most convincing proof of the existence of the X-ray bursts in a single event came from the long drift detector. The long drift detector operating condition was described in chapter 2.3. A fraction of the solid angle extended by the sensitive region of the long drift detector in this test was $\Delta\Omega/\Omega$~0.0019. Fig. 6a shows oscilloscope pictures of the X-ray events, which follow the initial spark noise. The relaxation oscillator was operating in air at V_{spark}~1.45kV and p~270μ. Fig. 6b shows similar X-ray production with argon at V_{spark}~2kV and p~170μ. For comparison, Fig. 6c shows a typical calibration pulse from the Fe^{55} X-ray source. Notice that the X-ray events appear in clusters (Fig. 6a,b). To study the single X-ray events, it is necessary to adjust their flux so that the probability to observe the X-ray pulse per spark was only ~10%, thus ensuring only a small probability of a pile-up from different events. This was achieved by placing an additional 178μm Mylar absorber in the X-ray path, creating a total Mylar thickness of 261μm between the spark and the sensitive volume of the long drift detector. The sparking vessel was filled with argon, and operated at V_{spark}~2kV and p~170μ at this point. The counting of X-ray pulses was done visually using a digital scope. Fig.7 shows a multiplicity distribution of the X-ray pulses per spark, indicating a mean of 3. Extrapolating this result to a 4π-solid angle and assuming an isotropic distribution, one would expect more than $3*(\Omega/\Delta\Omega)$~1500 X-ray pulses.

From a visual observation of scope traces, it appears that the average energy of the X-rays is below ~10keV. The signal disappears when placing either a 1.6mm thick lead sheet or even a 762μm thick Mylar sheet in front of the long drift detector (see the next chapter for a quantitative evaluation of average energy).

3.2. Average effective X-ray energy using a range measurement

An advantage of the range measurement is that it is simple and insensitive to any spark noise. We have used Mylar, Kapton, aluminum and stainless steel absorbers mounted in slide frames. The slides were carefully placed into a X-ray path between the sparking vessel and the detector. Fig. 8a shows a comparison of calculated and measured attenuation curves for the setup using the Geiger counter TBM-3S. The X-rays passed through a 12.7 μm thick stainless steel sparking vessel window, 3 cm of air and 38 μm of Mylar foil on the counter. The sparking vessel was operating with air at V_{spark}~2.1kV and p~240 μ. One can see that an average measured effective energy of X-rays is slightly above 4keV. For comparison, Fig. 8a also shows measured calibration data using the Fe^{55} source producing 5.9keV X-rays; it agrees fairly well with the calculation.

Fig. 8b shows a comparison of calculated and measured attenuation curves for the setup using the tube wire detector. In this case, the X-rays passed through a 12.7 μm thick stainless steel sparking vessel window, 3 cm of air and a 30 μm thick aluminized Mylar foil of the tube window. The sparking vessel was operating with air at V_{spark}~2.1kV and p~240 μ. Again, one can see that an average effective energy of X-rays is slightly above 4keV. Fig. 8b also shows the calibration data using the Fe^{55} source producing 5.9keV X-rays. Both methods, one using the Geiger counter and one using the tube wire detector, agree with each other.

The spark charge contains approximately ~10^{15} electrons. The question is what is the probability that one such electron creates an event, containing any number of X-ray pulses. Combining results with the long drift detector of chapters 3.1, and the tube detector of chapter 3.2, we calculate this probability as follows: ~0.1*5*10^{-15} = 5x10^{-16}, where 0.1 is the probability to observe an X-ray even per spark containing 10^{15} electrons, a factor 5 comes from the absorption correction caused by the 262 μm Mylar absorber in the X-ray path (see the multiplicity measurement in chapter 3.1), assuming an average X-ray energy ~4keV (Fig. 8b). To be able to see this phenomenon one needs a very large instantaneous spark current (>400A). For example, one would not see it using electrons from an ordinary β-source.

3.3. X-ray energy distribution

Difficulty to measure the pulse height distribution correctly in this experiment is mainly related to a short duty cycle of the X-ray production, and to a possible spark noise. The X-rays are produced within ~150-200ns time interval (see chapter 3.5), and they seem to occur in multiple events (see chapter 3.1). To make sure that we are dealing predominantly with the single X-ray pulses when measuring the pulse height spectra, we need to limit the probability of a single X-ray pulse per spark to less than 5%. This was achieved by: (a) restricting the X-ray flux with a ~1mm diameter hole in the 1.5mm thick lead sheet, (b) by running at the lowest possible sparking voltage. Despite these precautions, there is still a non-zero chance of having two X-ray pulses within the integration

gate, and therefore one should not over-interpret a maximum X-ray energy measured in the test. The maximum observed energy is also affected by a resolution of the detector, which has to be determined by a separate calibration run. The spark noise was reduced by careful shielding precautions (see chapter 2.3), and by running relatively long shaping time of the amplifier, which, however, made it more difficult to resolve doubles.

3.3.1. Wire tube detector with a long integration time constant.

We used a charge integrating amplifier with a gain ~50mV/pC and a shaping time ~20μs, and a digital oscilloscope to measure the pulse height spectrum by determining a peak of each pulse. In this way every pulse contributing to the pulse height spectrum was visually checked. The X-rays passed through a 51μm thick Mylar window of the sparking vessel, 3 cm of air and a 30μm thick aluminized Mylar foil of the wire tube window before there was a detection in the wire tube chamber operating with 95% Ar+5% CH_4 gas.

Fig. 9a shows uncorrected X-ray pulse height spectra in air, hydrogen, argon and xenon gases. The spark gap was operating at V_{spark}~0.9kV and p~310μ for air, at V_{spark}~1.55kV and p~950μ for hydrogen, at V_{spark}~0.8kV and p~240μ for argon, and at V_{spark}~1.81kV and p~135μ for xenon. One can see a cutoff due to absorption in window materials below ~3kV.

Using the calculated attenuation factors for each absorber in the X-ray path, and using the calculated wire tube detection efficiency based on the energy dependent attenuation factors in each component of the chamber gas (see equation 1, Ref. 6 and Fig. 5a), one can correct the measured spectra of Figures 9a, and obtain a shape of primary X-ray spectra at the source. Fig. 9b shows the final results for air, hydrogen, argon and xenon in the sparking vessel. The spectra have the same shape within the experimental errors, and they follow a power law distribution.

The scale was calibrated with the Fe^{55} radioactive source. The resolution σ/Peak of the wire tube detector was ~14% at 5.9 keV.

3.3.2. Wire tube detector with a short integration time constant.

In this test, the wire tube detector was coupled to the charge integrating amplifier with a gain ~15mV/pC and shaping time ~65ns. The pulse height spectrum was measured using the QVT pulse height analyzer operating in the charge integrating mode (q-mode) with an external gate 400ns long. The shape of the X-ray distribution and the maximum energy observed in argon and xenon were consistent with the results presented in Fig. 9a.

3.3.3. YAP scintillation detector with a short integration time constant.

In this test, the YAP scintillation detector was coupled to a PM operating at -1.4kV. The PM anode output was amplified by the charge integrating amplifier with a gain ~15mV/pC and shaping time ~65ns. The pulse height spectrum was measured using the QVT pulse height analyzer operating in q-mode with an external gate 400ns long.

In this case we were interested if there are some X-rays with much larger energies than ~10keV. Fig. 10a shows uncorrected X-ray pulse height spectrum in xenon on logarithmic scale. The spark gap was operating at V_{spark}~1.81kV and p~135μ. Fig.10b shows the same spectrum but in this case the X-rays were blocked with 1.5mm thick lead sheet. As expected, no events were observed above the pedestal peak. Fig.10c shows the calibration spectrum using the Cd^{109} radioactive source. The resolution σ/Peak of the YAP detector is only ~26% at 22 keV, which is expected due to a finite photoelectron statistics in this type of scintillator. This is a considerably worse resolution compared to the gaseous wire tube detector which is better suited for this application in this energy range. Taking into account the relatively poor resolution of the YAP detector, we conclude that the result of this measurement is consistent with the corresponding result from the wire tube detector in Fig. 9a. However, Fig.10a shows few events with energy up to 20-25keV, which would indicate a presence of larger energies compared to what we measured with the gaseous wire tube detector in Fig.9 (at X-ray energy of ~20keV the gaseous detector has practically zero detection efficiency - see Fig.5a).

3.4. X-ray production rate as a function of E/p, sparking voltage and gas

In this test, the X-rays passed through a 51μm thick Mylar window of the sparking vessel, ~3cm of air and the Geiger detector window (38μm thick Mylar), i.e. the X-rays below 2-3keV were absorbed. We placed additional Mylar absorbers in front of the detector to evaluate the hardness of the X-ray radiation. The gases in the sparking vessel were hydrogen, air, nitrogen, argon and xenon. We used the following gas pressure ranges: 195-230μ for argon, 120-140μ for xenon, 280-320μ for air, 275-330μ for nitrogen and 850-1020μ for hydrogen. Outside these pressure ranges, the X-ray production stopped, although the spark gap continued to glow. The X-ray production was accompanied by a characteristic spark sound, the glowing was quiet. Fig.11 shows measured X-ray rate in the Geiger detector as a function of the sparking voltage for several gases in the sparking vessel. Notice that the argon X-ray spectrum appears to be hardest in this group of gases.

Many gaseous phenomena depend on the E/N variable, where E is the electric field and N is number of molecules per cm^3. E/N is often approximated by a E/p variable, where p is the gas pressure. For example, the electron drift velocity is often expressed as a function of E/p. Unfortunately, it is difficult to know E precisely due to a dynamic behavior of the spark; the space charge effects must also be very important for charges ~10^{15} electrons per spark; for E/p higher than 10kV/cm/Torr, an electron energy is higher than ~50eV, causing ionization. Similarly, a spark pressure may not be known since it depends on the spark temperature, which was not measured directly during the test (a surface temperature of the sparking vessel was increased rapidly; within 30 minutes it climbed to 70-80°C). Therefore, only approximations can be made. We assume that

$E = V_{spark}/d$, where V_{spark} is determined from Fig.2c and d is ~1 mm, and p is the gas pressure monitored ~20cm away from the sparking vessel.

Fig. 12a shows measured X-ray rate in the Geiger detector as a function of E/p value for several gases in the sparking vessel. In this measurement, no additional absorber was placed between the sparking vessel and the detector. One can see that hydrogen starts producing the X-rays at lowest E/p, xenon at highest. From Fig. 12b it appears that the X-ray production threshold correlates with the Z of the gas.

Fig.13 shows the result in air at sparking voltage V_{spark}~0.9kV. We see an increase in rate as a function of elapsed time since the beginning of the sparking. This may be related to an increase in the sparking temperature, which changes E/p. To minimize systematic errors in relative comparison of different gases, we decided to wait typically one hour before starting each measurement.

3.5. The X-ray production and the I, V and dI/dt dependence of the spark

We have added several components to the setup of Fig.1 to measure I(t), V(t) and dI/dt(t) spark parameters. The current I(t) was measured with a 1.2Ω shunt resistor placed in ground return of the spark gap, the voltage V(t) was measured with a simple 1000:1 divider and the current derivative dI/dt(t) was measured using the toroid coil (so called Rogovski coil [7]). The coil was placed around a conductor delivering the current into the spark gap; it had 30 turns, minor radius 4.2mm and major radius ~17.8mm. To check the Rogovski coil measurement, we have also performed a numerical derivative of the I(t) curve, and both agree. Fig.14 shows the time development of current, voltage and dI/dt during the spark and the timing of the X-ray production relative to them; the X-rays were measured in the wire tube detector.

We observe the first X-rays about ~150ns after the spark starts and they are all contained within a time interval lasting 150-200ns, which corresponds to an observation of a slight dip in current I(t). The current dip corresponds also to the largest swing of the dI/dt(t). The voltage measurement shows a small ripple during this time; however we did not measure larger values than the expected spark voltage V_{spark}. The observation of the X-ray production during the dip in current appears to be consistent with what is observed during the pinch effect studies [1-4].

4. DISCUSSION OF THE PRODUCTION MECHANISM OF THE X-RAYS

We clearly see the production of soft X-rays with energies between 2 and 10keV, which are above the expected value based on the known sparking voltage. They occur during a slight dip in current I(t). This observation appears to be consistent with the earlier pinch effect studies [1-4], which are explained in the plasma field using the theory of radiation collapse [1].

However, one should stress that our spark energies at our smallest sparking voltage (~0.8kV) are at least a factor of ~4×10^4 smaller compared to the spark energies used in Ref.1-4. If we really

observe the pinch effect it is occurring at the smallest spark energy reported so far in literature, and we would be then investigating the behavior of its threshold. The maximum observed X-ray energy (~10keV), generated at the lowest voltage (~0.8kV), is more than ten times than expected; and it is above K-shell energy of typical gases we used in our tests, or materials used in our spark electrodes (see Table 1 and chapter 4). The X-ray production persists even for the carbon electrodes which have the smallest K-shell energy (0.284keV); this would appear to eliminate a theory that the electrode atoms are responsible for the X-ray production. Furthermore, we have the evidence that the production threshold and the X-ray rate is dependent on the gas choice in the sparking vessel. Because of the doubts that the pinch effect is the only explanation for the observed phenomenon, we were interested to search for other possible explanations:

(a) The first obvious question is if our spark voltages could produce characteristic K-shell X-rays in materials or gases present in our system assuming a multi-electron participation on a liberation of a K-shell electron of some heavy atom such as iron, nickel or molybdenum (see Table 1). This would be a phenomenon similar to the double-photon ionization of gas impurities observed when a UV laser is shining into a gaseous drift chamber. However, it appears to us that such a production is very unlikely; it is difficult for a charged electron, having an energy of only 50-100eV, to penetrate deeply inside the atom compared to a neutral photon during the multi-photon excitation; furthermore, it would take more than five electrons to participate in one single event to ionize the K-shell electron. To eliminate this possibility experimentally, we decided to use the carbon electrodes in the spark gap. The insulator was made of nylon to eliminate the porcelain[5] which could, in principle, contain some ferro-electric crystals. We repeated the production of soft X-rays with this arrangement under similar experimental conditions as discussed in this paper. This indicates that the soft X-ray production is very likely related to the gaseous phenomenon, and not to the spark gap material or the insulator properties.

(b) In principle, the hot plasma can excite the X-rays through the phenomenon of "thermal bremsstrahlung", which is caused by the electron-ion collisions at extremely high temperatures. It is necessary to heat a plasma to temperatures between 10^7 and 10^8 ^oK to excite the X-ray spectra of Fig. 9b. We exclude this possibility in our experiment because the predominant radiation from the spark is in the visible spectrum and therefore the average temperatures we are dealing with are very likely below 10^4 ^oK.

---

[5] According to Dr. B. Manning of Champion Co., the porcelain in their spark plug (J-12Y) does not contain the ferro-electric crystals; The spark plug electrodes are made of an alloy of Ni, Cr, Ma, Si, Ti, Zi and traces of C and Fe; the ceramic insulator is made of Al_2O_3 (~90%) and glass phase made of clay containing impurities of Ti, Ca, Na, Fe, Zi, etc.).

(c) One also cannot exclude that there is a new physics, which goes either in parallel to the theory of the pinch effect, or is driven by it, or even drives it. Refs. 8-12 suggest that both relativistic Schroedinger and Dirac wave equations allow that atoms may have additional energy levels (so called Deep Dirac levels or DDL levels, which correspond to electron orbits close to nucleus). If such atomic levels indeed exist then the plasma environment of the spark may be an ideal place to excite such transitions, because of a large number of ions and energetic electrons involved. A free energetic electron, perhaps even driven by the pinch effect, may enter an ion with such a velocity that it is captured by the new DDL atomic energy level. During such entry to the DDL level the electron will radiate the Bremstrahlung spectrum involving many photons, some of them would be X-rays (for example, for hydrogen the total energy released is close to ~509keV).

So far we have not established a proof that the DDL atoms exist. However, we continue in this search and have finished building a larger detector capable of detecting the soft X-rays over a larger solid angle. The aim of this search is two-fold: (a) verify that the X-ray production is indeed isotropic, which must be an essential characteristic of the DDL atomic transitions (as opposed to the pinch effect), (b) make a better estimate of the total energy sum per one single event. The DDL events would have a definitive signature: a large number of isotropically distributed X-rays with the total energy sum approaching ~0.5 MeV.

One may apply the results of this work to explain the soft X-ray spectra from various stars. For example, Fig. 15a shows a recent astronomical data of the X-ray flux originating from an object called PKS2155-304 as measured by a satellite BeppoSAX, equipped with the soft X-ray detectors [13]. Fig.15b shows the background spectrum from Crab Nebula, which is used for a normalization. Ref.13 speculates that the origin of these spectra is the Synchrotron emission. However, it is possible to explain, at least in principle, the shape of the spectrum of Fig.15a using a composition of spectra similar to those of Fig. 9b from many contributing elements, i.e. using the plasma processes similar to those investigated by this work as the origin of the soft X-rays from these objects.

CONCLUSIONS

1. We observe the production of soft X-rays of energy 2-10keV by sparking in hydrogen, air, nitrogen, argon and xenon gases at low pressure with a sparking voltage as low as 0.8-1.6kV.
2. The X-ray events appear to come in clusters, with an average mean multiplicity of 3 per event into the solid angle of our long drift detector. The extrapolated production into a 4π-solid angle is more than ~1500 pulses, assuming the isotropic distribution.
3. The X-ray pulse height spectra in all tested gases have similar shape resembling a power law distribution between 2 and 10 keV. Using the range method, the average measured X-ray

energy is about 4keV.

4. The X-ray production threshold depends on E/p of the spark chamber gas. The threshold value increases as the gas Z increases.
5. The X-ray production persists even for the carbon electrodes; this would appear to eliminate a theory that the electrode atoms are responsible for the X-ray production.
6. We calculate that a probability to produce an X-ray event per one electron in a given spark is less than ~$5x10^{-16}$. To be able to see this phenomenon one needs a very large current. One would not see it with electrons from an ordinary β-source.
7. The paper also suggest that the observed X-rays could come, at least partially, from a new process, where energetic free electrons enter ions and are captured on the DDL levels [8-12] radiating the Bremstrahlung spectrum involving many photons.

ACKNOWLEDGMENTS

We are grateful to Catherine Maly for editing this paper. We would like to thank Dr. S. Majewski for providing the YAP scintillator for this test.

FIGURE CAPTIONS

1. Our experimental setup for sparking in gases at low pressure. It uses a spark plug with a 1 mm gap, operating as a relaxation oscillator.
2. (a) We used a special voltage divider, equipped with a capacitive correction, to determine: (b) a sparking voltage V_{spark} and a sparking period T. (c) A calibration curve correlating the sparking voltage V_{spark} and the spark period T.
3. Geometry of the single wire proportional tube detector including its spark noise shield.
4. Geometry of the long drift detector.
5. Calculated attenuation curves for various materials in the X-ray path, and an expected X-ray detection efficiency for (a) the tube wire chamber and (b) the long drift detector. The attenuation calculated for 51 μm thick Mylar sparking vessel window (diamonds), 3 cm of air (squares), 33 μm (tube) or 12.5 μm (long drift) wire chamber window (triangles), the combined attenuation factor (x) and the final detection efficiency (star).
6. (a) A cluster of X-ray pulses detected in the long drift detector; sparking in air at a sparking voltage V_{spark} ~1.45kV and a pressure ~270 μ; (b) A cluster of X-ray pulses detected in the long drift detector; sparking in argon at a sparking voltage V_{spark}~2kV and a pressure ~170 μ; (c) A calibration pulse from an Fe^{55} X-ray source for the same gas gain.

7. An average X-ray multiplicity per spark in argon, sparking voltage V_{spark}~2kV and pressure ~170 μ. The X-ray energy was between 3 and 10keV in average, and probability to observe an X-ray pulse per given spark was kept at only ~10% to ensure a proper X-ray counting.
8. (a) A comparison of a range measurement and calculated attenuation curves using the Geiger counter TBM-3S. The sparking data (open triangles) were obtained with air at sparking voltage V_{spark} ~2.1kV and pressure of 240 μ, a calibration was done using Fe^{55} X-ray source (open diamonds), calculation was done at 6keV (open squares), 5keV (open circles), 4keV (filled squares) and 3keV (filled circles). (b) The same for the tube wire detector. The sparking vessel was operating with air at sparking voltage V_{spark}~2.1kV and pressure of 240 μ.
9. (a) A measured X-ray pulse height spectrum using the wire tube detector while sparking in, air at ~0.9kV; hydrogen at ~1.55kV; argon at ~0.8kV; xenon at ~1.81kV. The X-rays passed through the 51 μm Mylar window in the sparking vessel, 3 cm of air and a 30 μm thick aluminized Mylar foil in the wire tube chamber. The energy scale was calibrated using the Fe^{55} source; the resolution σ/Peak of the wire tube detector is ~14% at 5.9 keV. (b) The same pulse height spectra as in Figures 9a, but corrected for the attenuation factors in various materials and the wire tube X-ray detection efficiency (see Fig.5a).
10. (a) A measured X-ray pulse height spectrum using the YAP scintillation detector while sparking in xenon at ~1.81kV. The X-rays passed through the 51 μm Mylar window in the sparking vessel, 3 cm of air and a 30 μm thick aluminized Mylar foil in the wire tube chamber (log vertical scale). (b) The same but the X-rays blocked with 1.5mm thick lead sheet (log vertical scale). (c) Calibration with a Cd^{109} radioactive source producing 22keV X-rays; the measured resolution σ/Peak is ~26% at 22 keV (linear vertical scale). Every 50-th count is bright.
11. Rate of the X-rays in the Geiger detector as a function of the sparking voltage V_{spark}, gas and a Mylar absorber thickness: (a) hydrogen, (b) air, (c) nitrogen and (d) argon; no absorber (diamond) and Mylar absorbers of the following thickness: 127 μm (square), 254 μm (triangle), 356 μm (filled circle), 483 μm (x), 610 μm (filled circles) and 711 μm (cross).
12. (a) The production threshold and the rate dependence of the X-rays in the Geiger detector on E/p value of the gas in the sparking vessel. (b) The dependence of the X-ray production threshold on Z of the gas in the sparking vessel.
13. The measured X-ray production rate as a function of elapsed time, in air at sparking voltage V_{spark}~0.9kV. The increase is due to the heating of gas which changes E/p.
14. Measured time development of the current I(t), voltage V(t) and current derivative dI/dt(t) relative to the X-ray production during our sparking tests. The X-ray burst lasts about 150ns and occurs about ~250ns after the spark starts. The spark gap was operating in this case in air

at V_{spark}~1.4kV and pressure ~290 μ; similar shape was measured at V_{spark}~0.9kV.

15. (a) The recent astronomical data of the X-ray flux originating from an object called PKS2155-304 as measured by a satellite BeppoSAX, equipped with the soft X-ray detectors [8]; (b) the same for CRAB Nebula used for the normalization purpose in (a).

REFERENCES

[1] K.N. Koshelev and N.R. Pereira, J. Appl. Phys., 69(1991)R21.

[2] L. Cohen et al., J. of the Optical Soc. of America, 58(1968)843.

[3] E.D. Korop et al., Sov. Phys. Usp. 22(1979)727, page 729.

[4] G. Herziger et al., Phys. Lett., A64(1978)390.

[5] H. Pruchova and B. Franek, Nucl. Instr & Meth., A366(1995)385; Issue of ICFA Instrumentation Bulletin, SLAC-PUB-7376, 1997; and H. Pruchova's Ph.D. thesis, Prague Tech. Univ.

[6] E. Storm and H.I. Israel, "Photon cross-section from 1keV to 100MeV for Elements Z=1 to Z=100", Atomic Data and Nucl. Data Tables 7(1970)565.

[7] For description of the Rogovski coil see for example S. Glasstone and R.H. Lovberg, "Controlled Thermonuclear Reactions," 1960, D. Van Nostrand Co., Inc., page 164.

[8] J. A. Maly, J. Va'vra, "Electron Transitions on Deep Dirac Levels I", Fusion Technology 24, 307, (1993).

[9] J. A. Maly, J. Va'vra, "Electron Transitions on Deep Dirac Levels II", Fusion Technology 27, 59, (1995).

[10] J. A. Maly, J. Va'vra, "Electron Transitions on Deep Dirac Levels III. Electron densities in hydrogen-like atoms using the relativistic Schroedinger equation", Submitted to Fusion Technology, November 2, 1994.

[11] J. A. Maly, J. Va'vra, "Electron Transitions on Deep Dirac Levels IV. Electron densities in the DDL atoms", Submitted to Fusion Technology, September 11, 1995.

[12] J. A. Maly, J. Va'vra, "Electron Transitions on Deep Dirac Levels V. Negative energies in Dirac equation solutions give double deep Dirac levels (DDDL)", Submitted to Fusion Technology, February 8, 1996.

[13] F. Frontera et al., Proceedings of Compton GRO Symposium, Williamsburg, 1993; P. Giommi et al., Astronomy and Astrophysics, May 28, 1997

Table 1 - Characteristic X-ray energies in keV of some elements which could exist in the vicinity of the spark either in the gas or on the surfaces of the electrodes (either a primary element or a contamination); data from Handbook of Chemistry and Physics, Published by the Chemical Rubber Co., Cleveland, Ohio, 1971, page E-178.

Z	Element	K	L_1	L_2	L_3	M_1	N_1
6	Carbon	0.284					
7	Nitrogen	0.400					
8	Oxygen	0.532					
13	Aluminum	1.556	0.087	0.072			
14	Silicone	1.838	0.118	0.0077			
15	Phosphorus	2.142	0.153	0.128			
17	Chlorine	2.822	0.238	0.202	0.201	0.0297	
18	Argon	3.200	0.287	0.246	0.244	0.035	
20	Calcium	4.038	0.399	0.350	0.346	0.0471	
22	Titanium	4.966	0.530	0.462	0.456	0.0605	
24	Chromium	5.988	0.679	0.584	0.574	0.0762	
25	Manganese	6.542	0.762	0.656	0.644	0.0817	
26	Iron	7.113	0.849	0.722	0.709	0.0937	
28	Nickel	8.337	1.02	0.877	0.858	0.111	
40	Zirconium	17.998	2.533	2.308	2.224	0.432	0.0516
42	Molybdenum	20.003	2.869	2.630	2.525	0.509	0.0692
54	Xenon	34.551	5.448	5.103	4.783	1.14	0.208

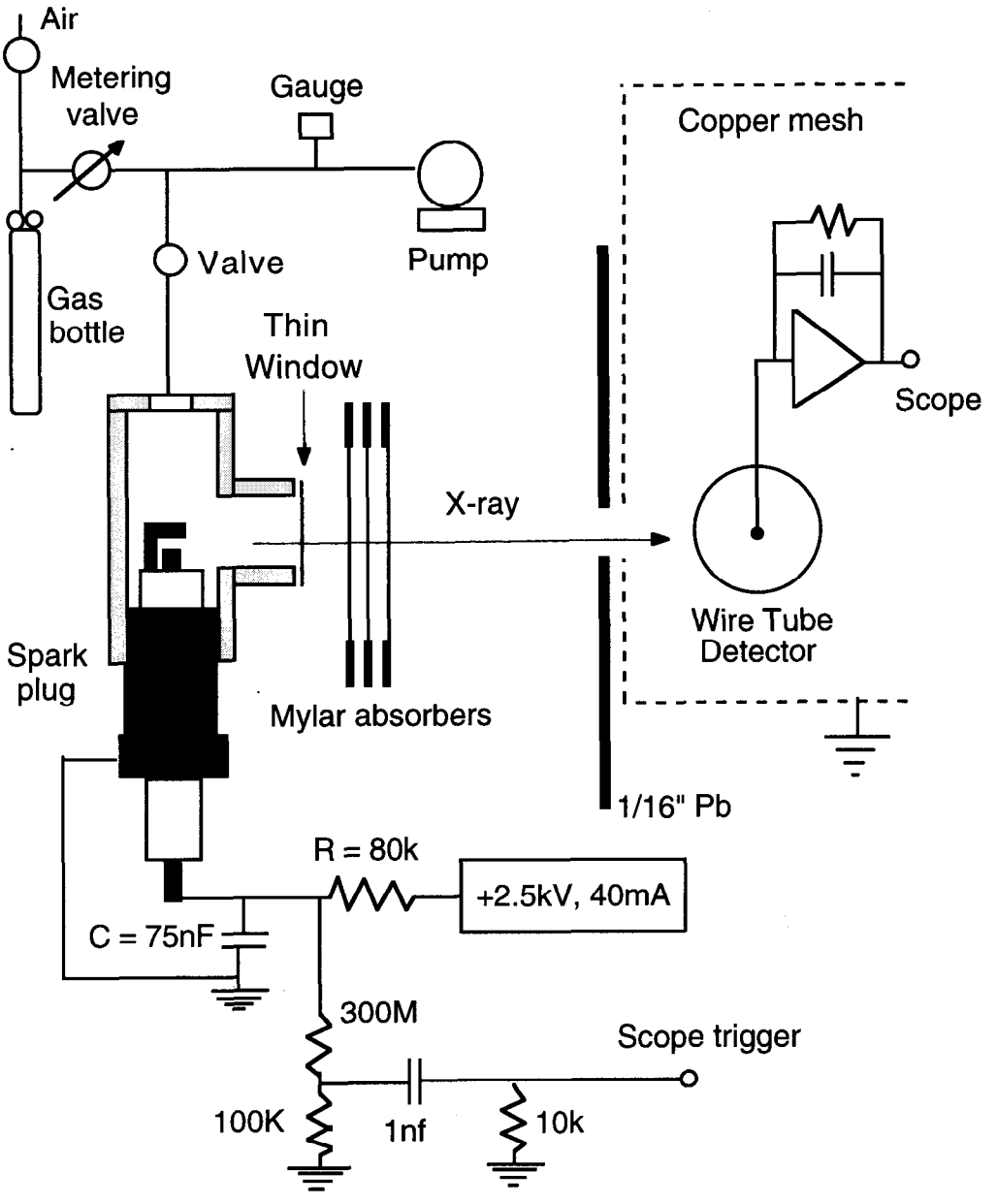
Air
Metering valve
Gauge
Copper mesh
Valve
Pump
Gas bottle
Thin Window
Scope
X-ray
Wire Tube Detector
Spark plug
Mylar absorbers
1/16" Pb
R = 80k
+2.5kV, 40mA
C = 75nF
300M
Scope trigger
100K
1nf
10k

Fig. 1

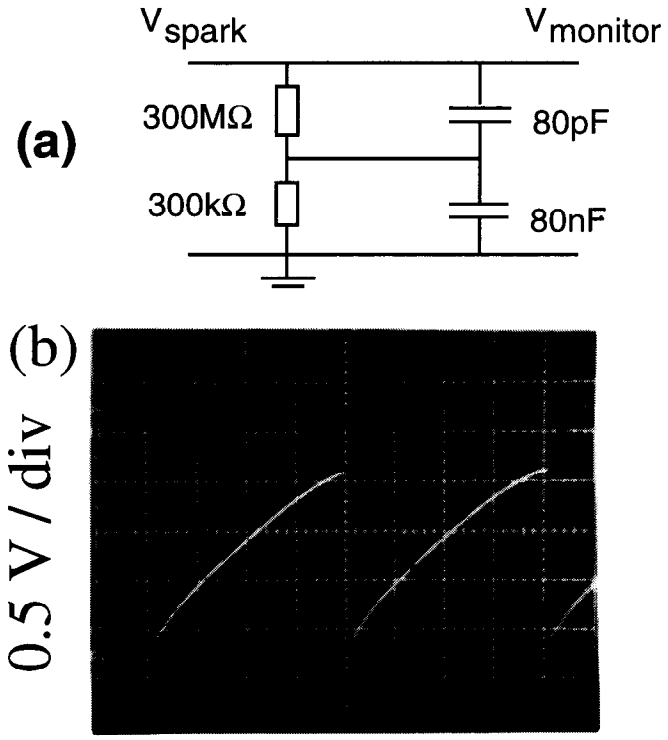
(a)
V_{spark}
$V_{monitor}$
300MΩ
80pF
300kΩ
80nF
(b)
0.5 V / div
5 msec / div
(c)
Spark voltage [kV]
2.5
2.25
2
1.75
1.5
1.25
1
0.75
0.5
4
6
8
10
12
14
16
18
20
Spark period [msec]

Fig. 2

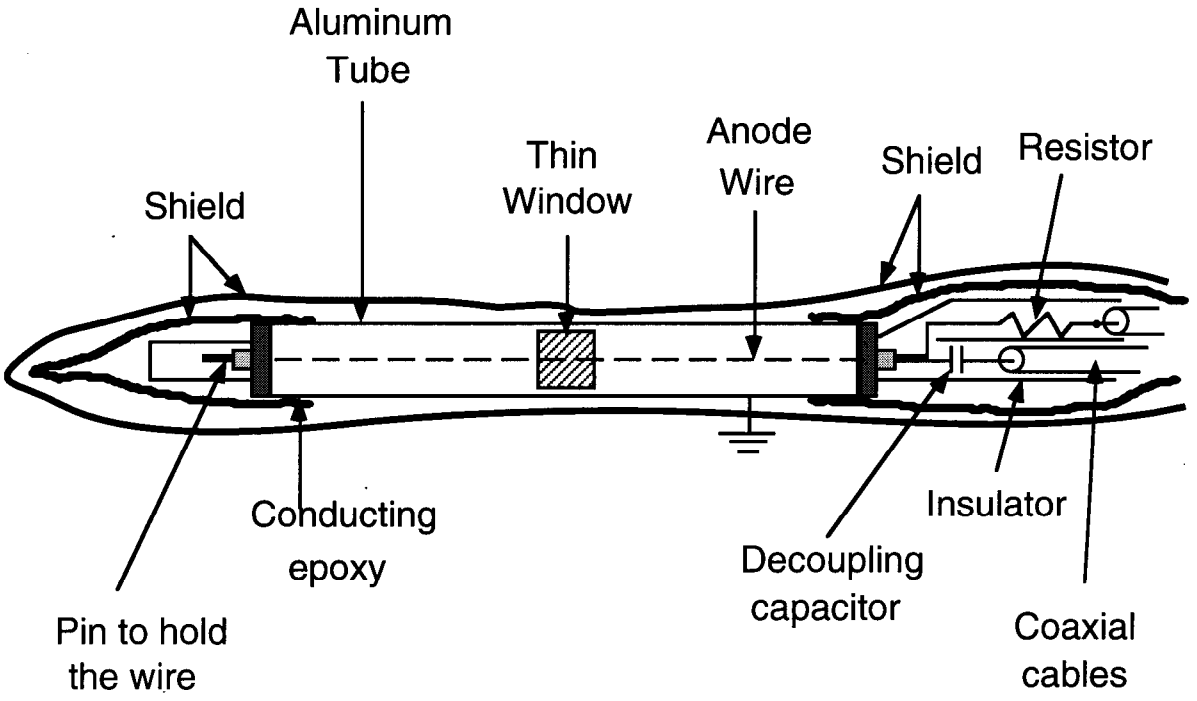
Aluminum
Tube
Shield
Thin
Window
Anode
Wire
Shield
Resistor
Conducting
epoxy
Insulator
Decoupling
capacitor
Pin to hold
the wire
Coaxial
cables

Fig. 3

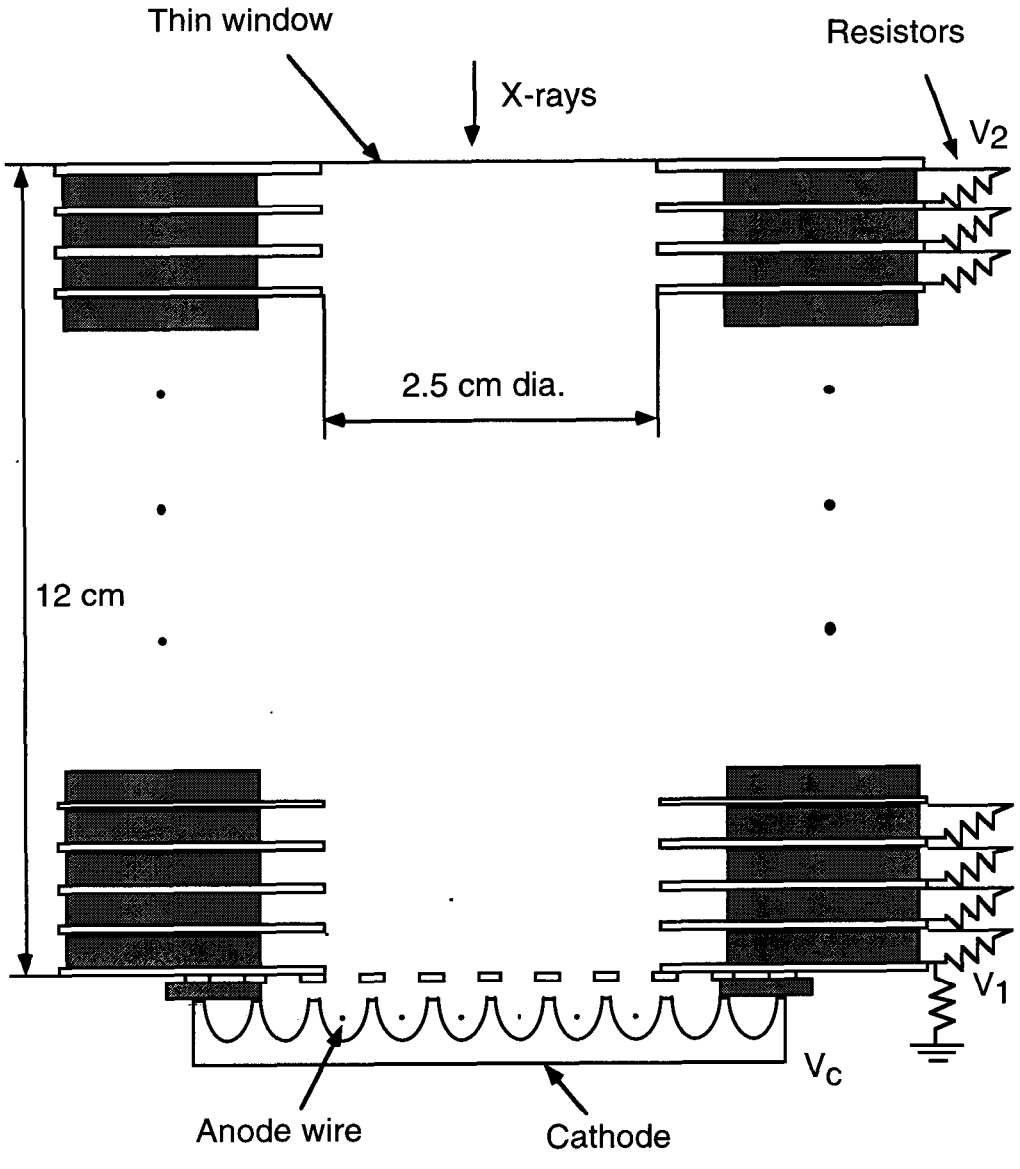
Thin window
X-rays
Resistors
V_2
2.5 cm dia.
12 cm
V_1
V_c
Anode wire
Cathode

Fig. 4

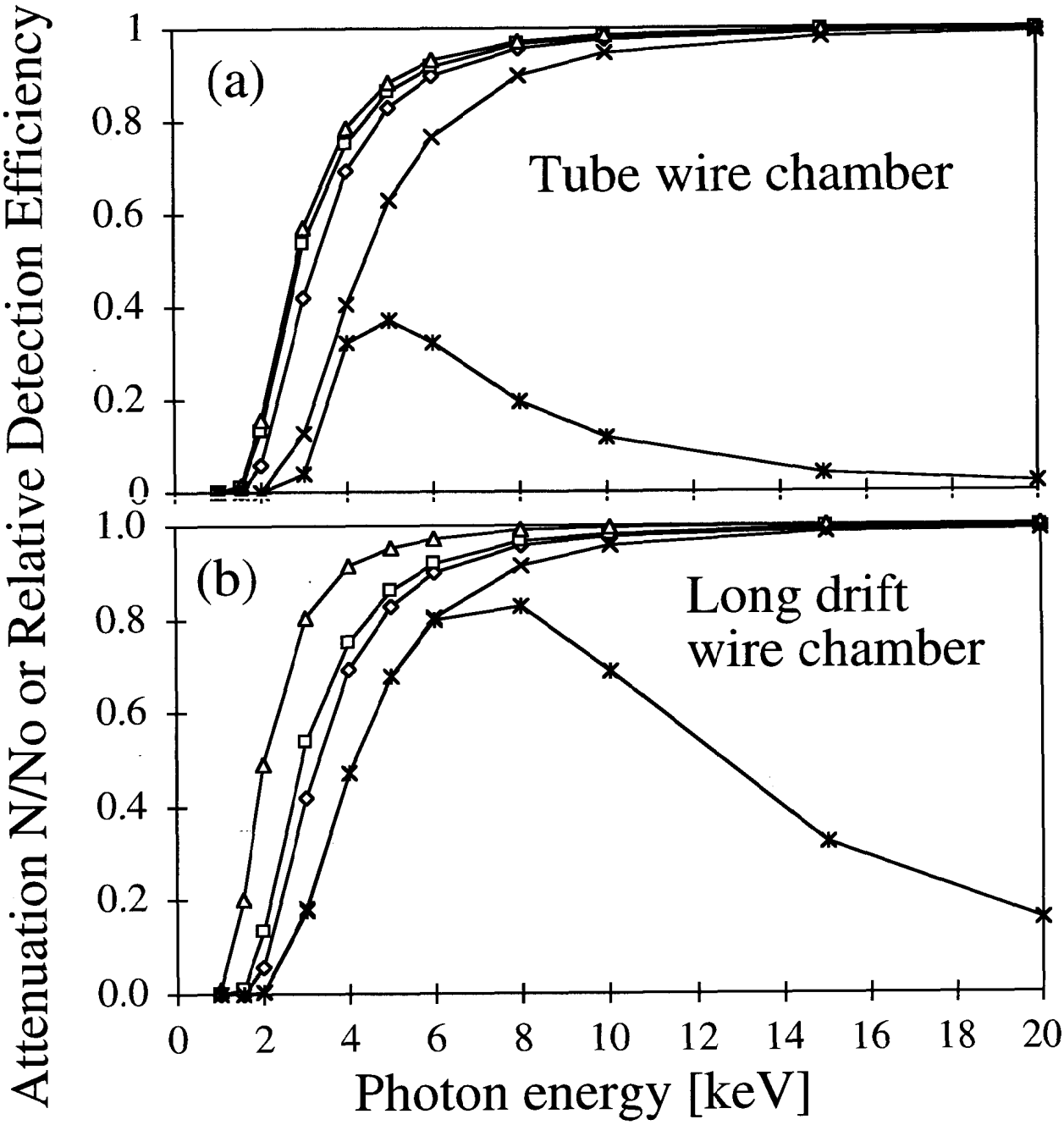
Attenuation N/No or Relative Detection Efficiency
(a)
Tube wire chamber
(b)
Long drift
wire chamber
Photon energy [keV]
0
0.2
0.4
0.6
0.8
1
1.0
0.0
2
4
6
8
10
12
14
16
18
20

Fig. 5

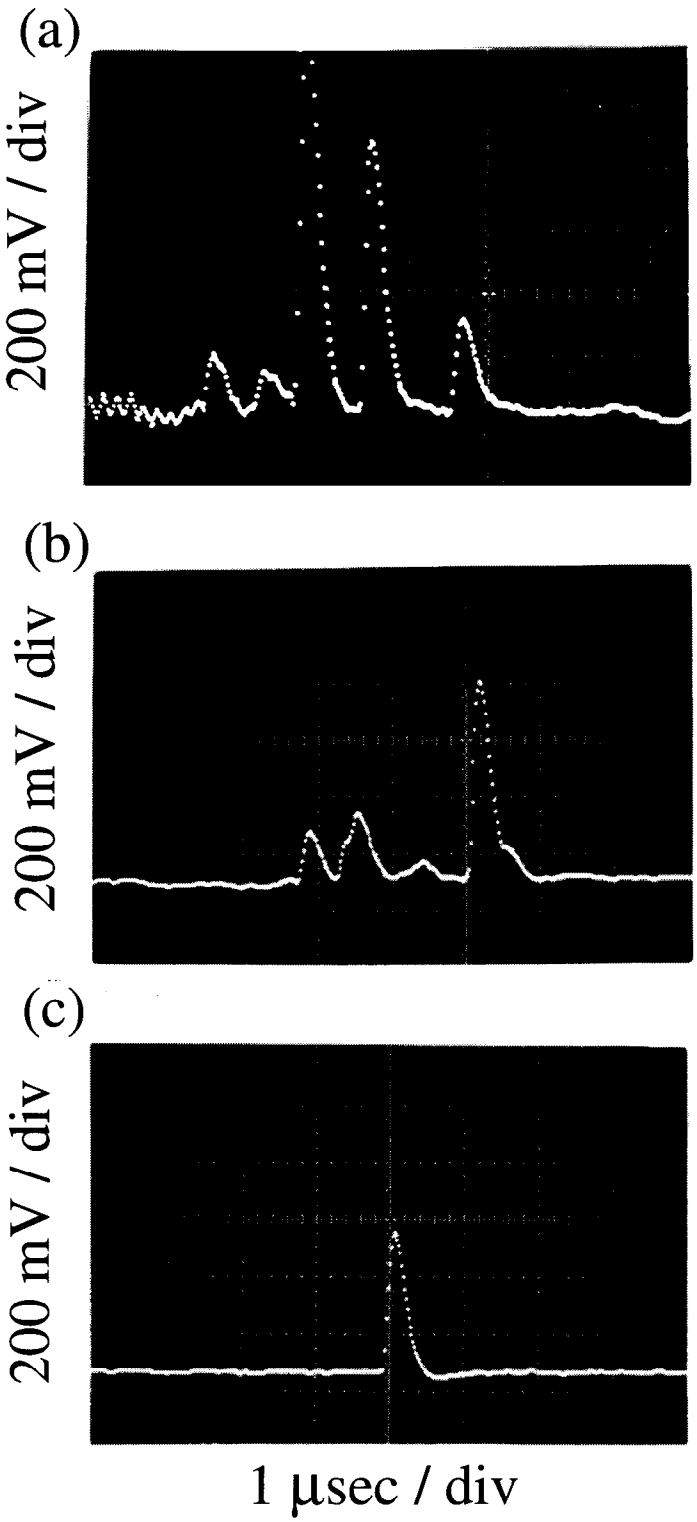

Fig. 6

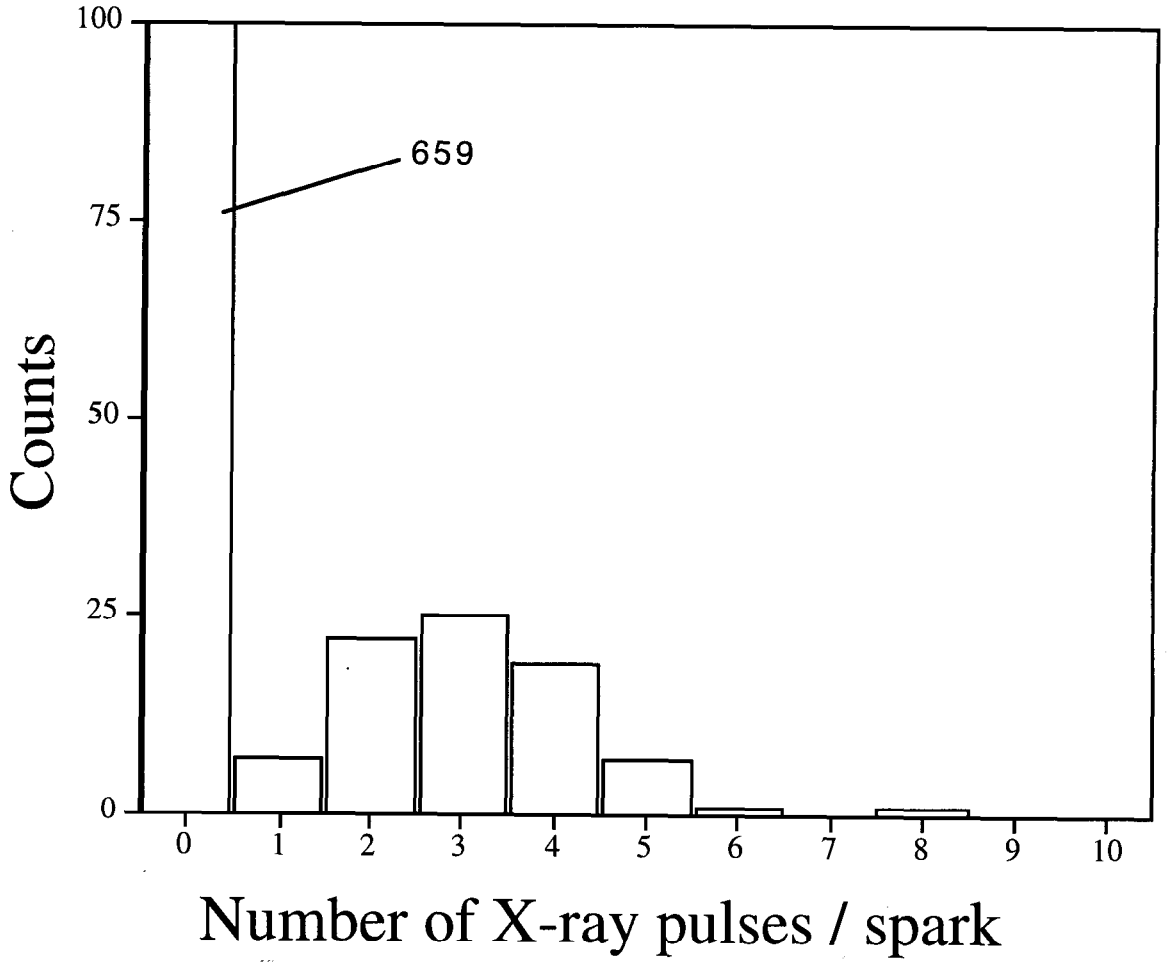
100
75
50
25
0
659
Counts
0
1
2
3
4
5
6
7
8
9
10
Number of X-ray pulses / spark

Fig. 7

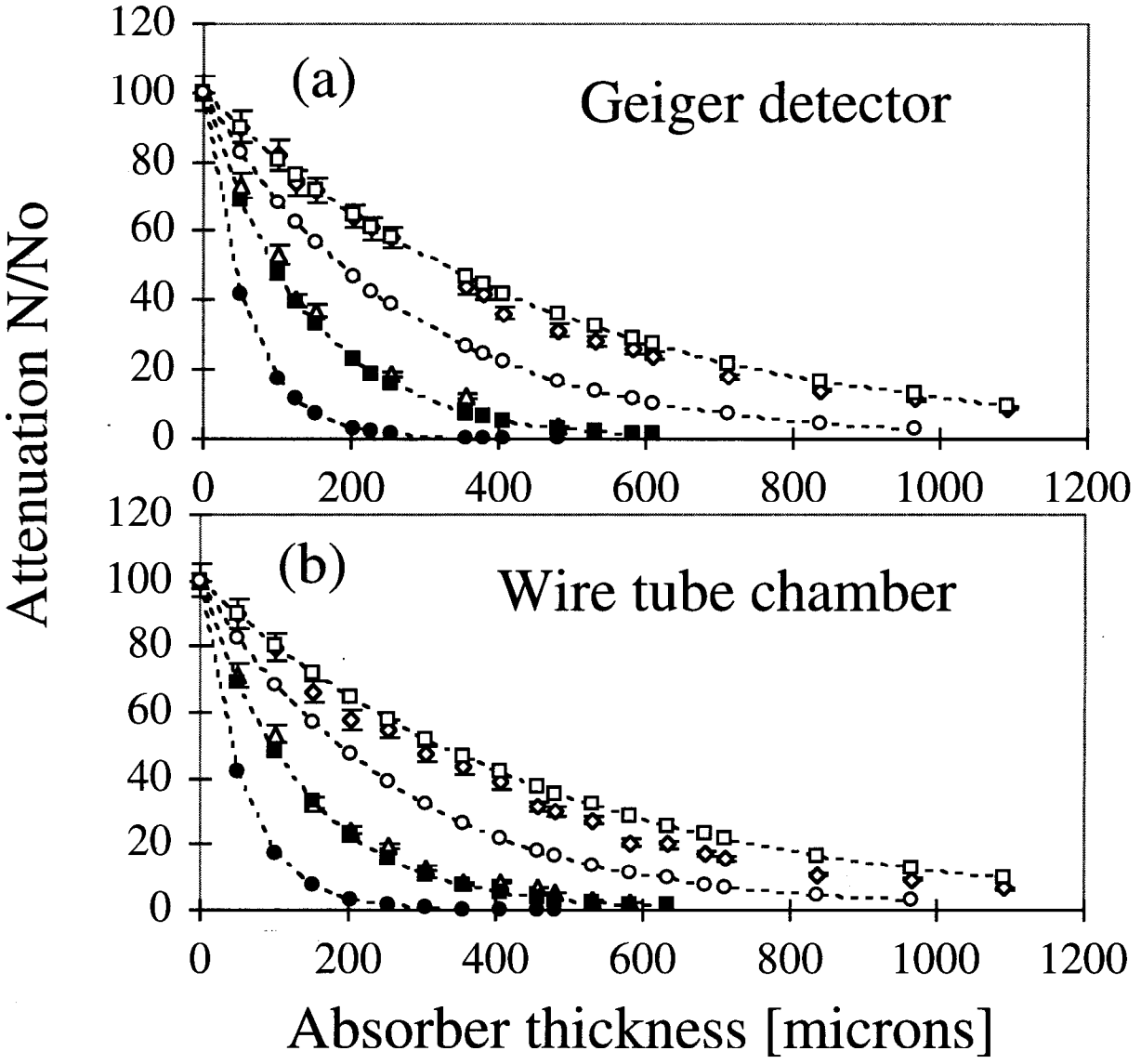
(a)
Geiger detector
(b)
Wire tube chamber
Attenuation N/No
Absorber thickness [microns]
0
20
40
60
80
100
120
0
200
400
600
800
1000
1200

Fig. 8

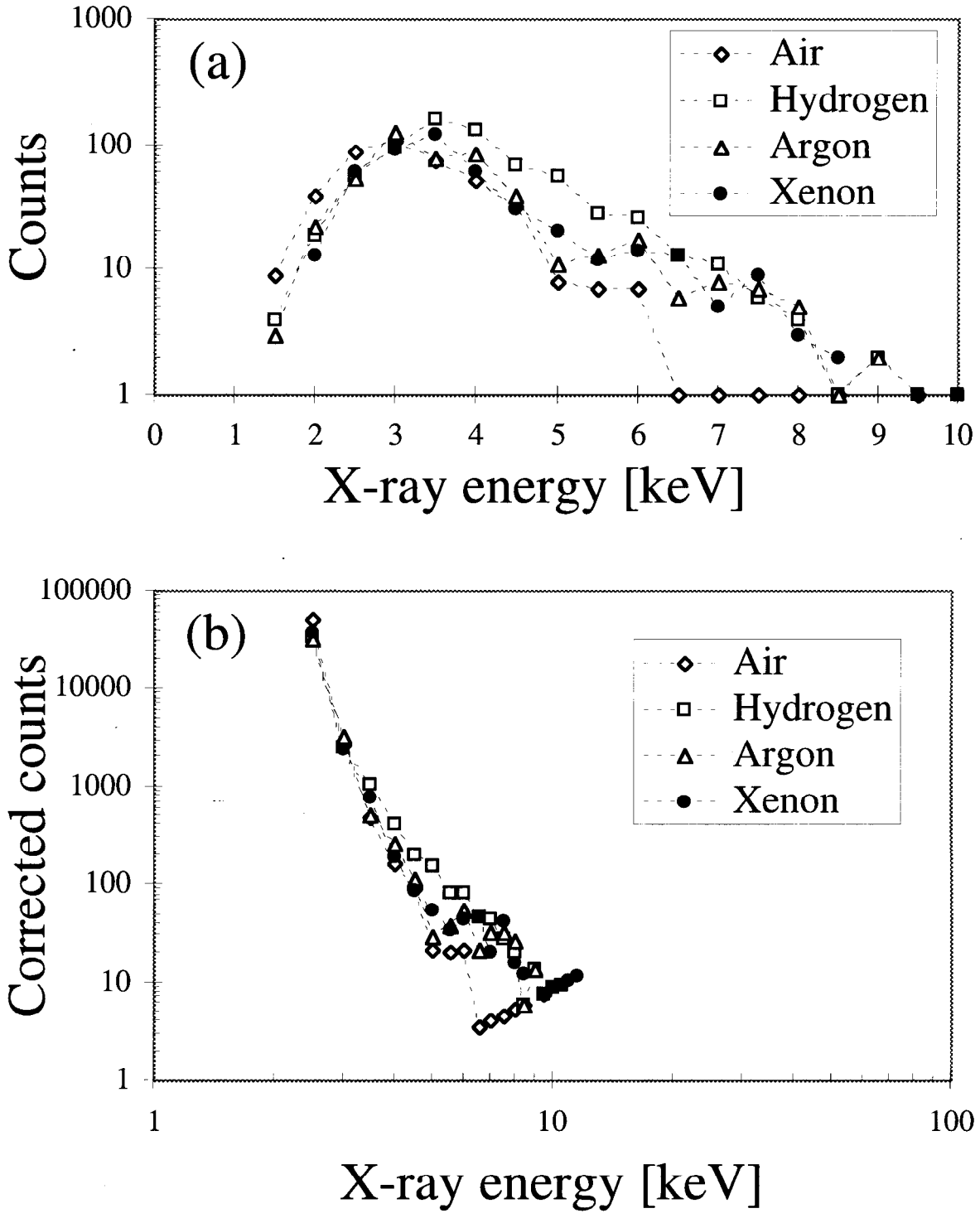
(a)
Air
Hydrogen
Argon
Xenon
Counts
1000
100
10
1
0
1
2
3
4
5
6
7
8
9
10
X-ray energy [keV]
(b)
Air
Hydrogen
Argon
Xenon
Corrected counts
100000
10000
1000
100
10
1
1
10
100
X-ray energy [keV]

Fig. 9

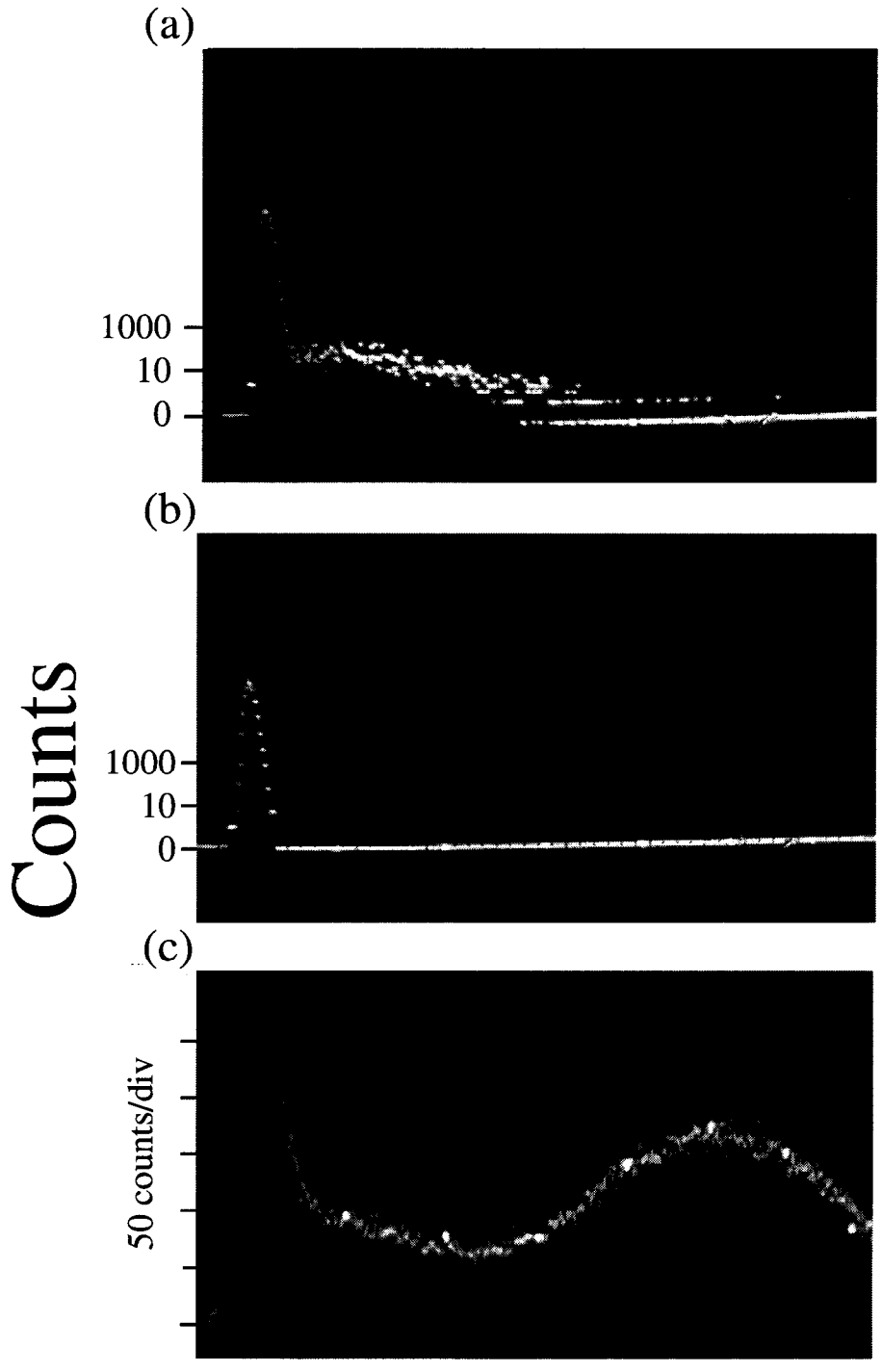
(a)
1000
10
0
(b)
1000
10
0
Counts
(c)
50 counts/div
X-ray energy [3 keV/div]

Fig. 10

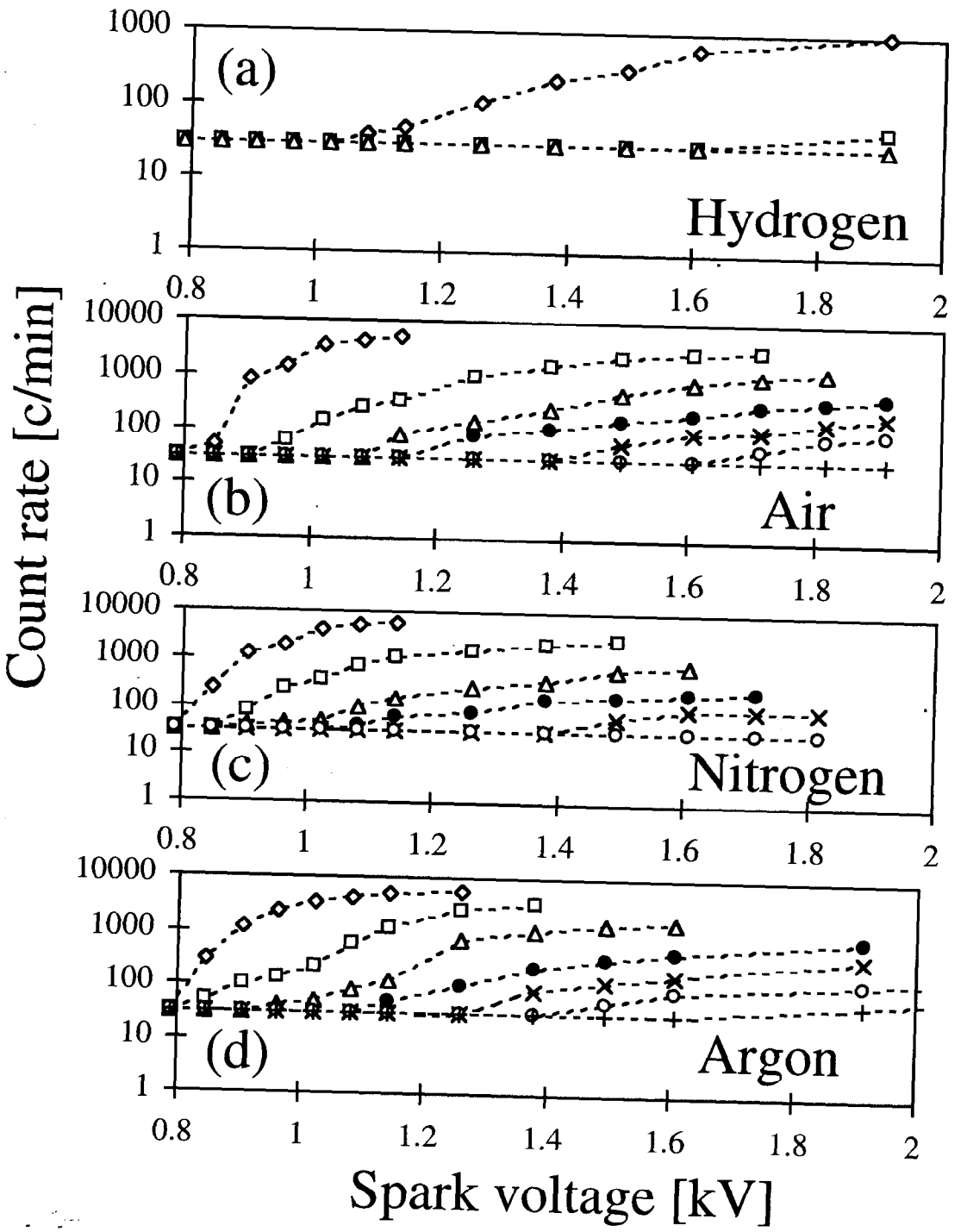
Count rate [c/min]
(a)
Hydrogen
(b)
Air
(c)
Nitrogen
(d)
Argon
1000
100
10
1
10000
0.8
1
1.2
1.4
1.6
1.8
2
Spark voltage [kV]

Fig. 11

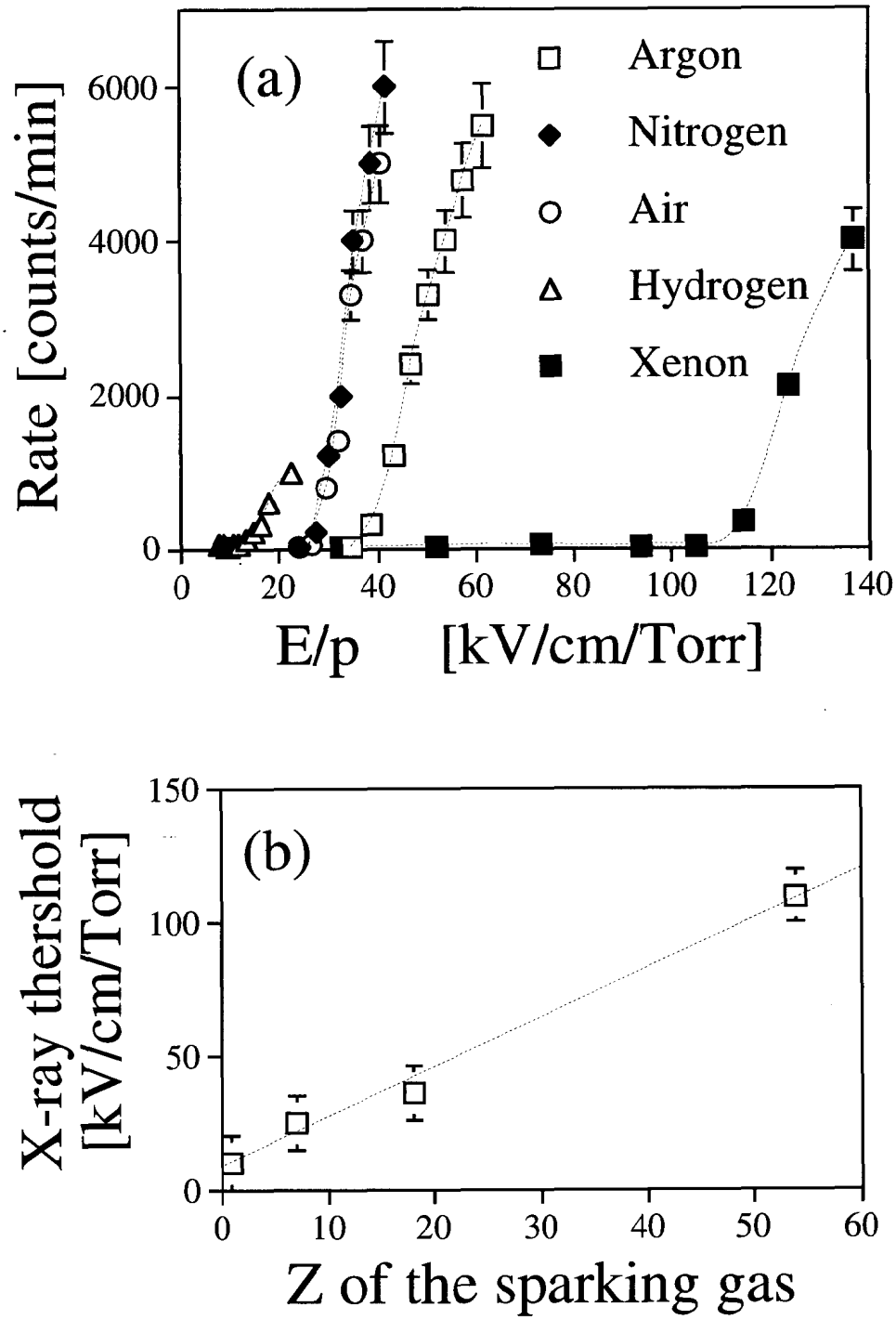
(a)
Argon
Nitrogen
Air
Hydrogen
Xenon
Rate [counts/min]
6000
4000
2000
0
0
20
40
60
80
100
120
140
E/p [kV/cm/Torr]
(b)
X-ray thershold [kV/cm/Torr]
150
100
50
0
0
10
20
30
40
50
60
Z of the sparking gas

Fig. 12

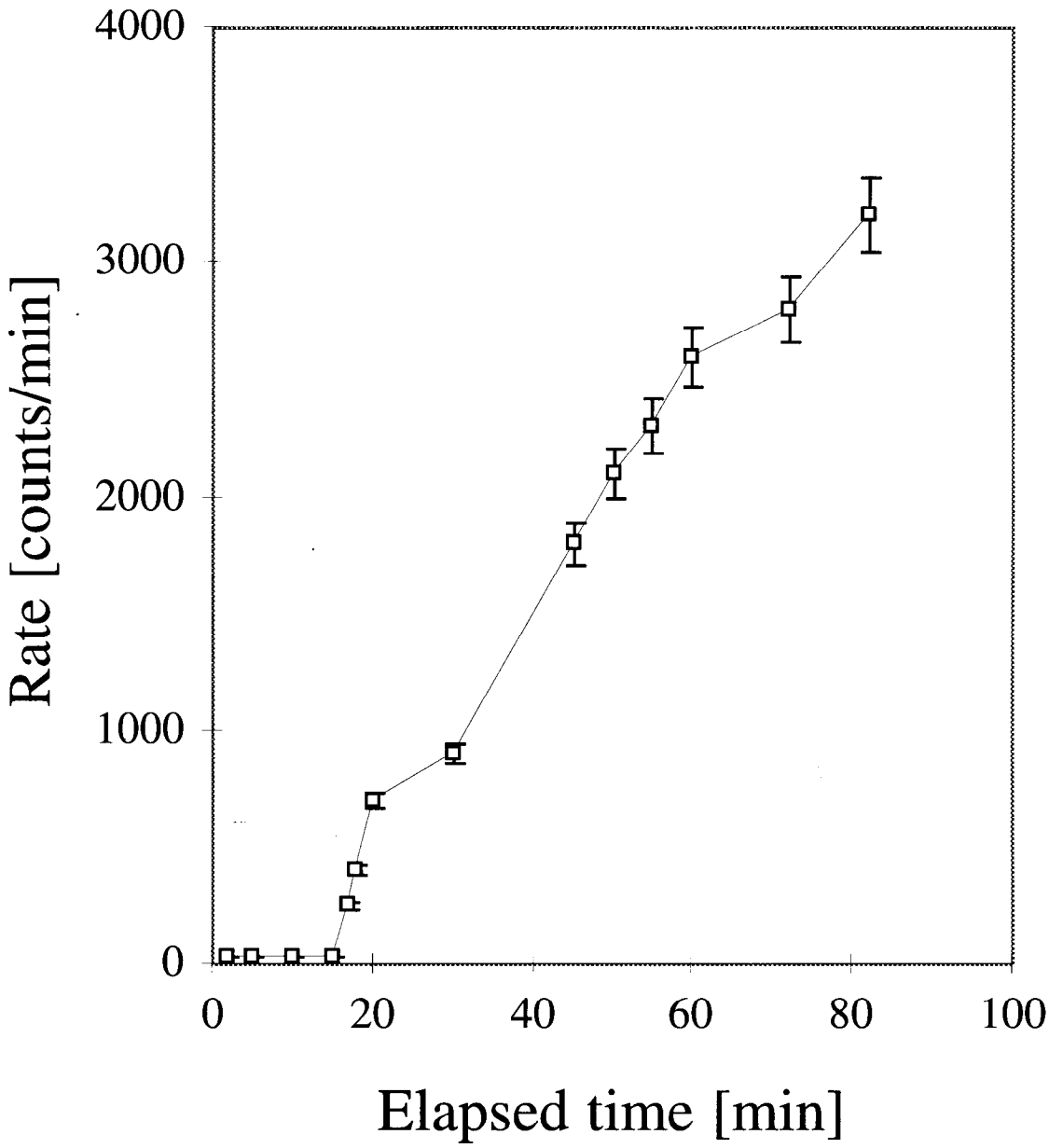
4000
3000
2000
1000
0
Rate [counts/min]
0
20
40
60
80
100
Elapsed time [min]

Fig. 13

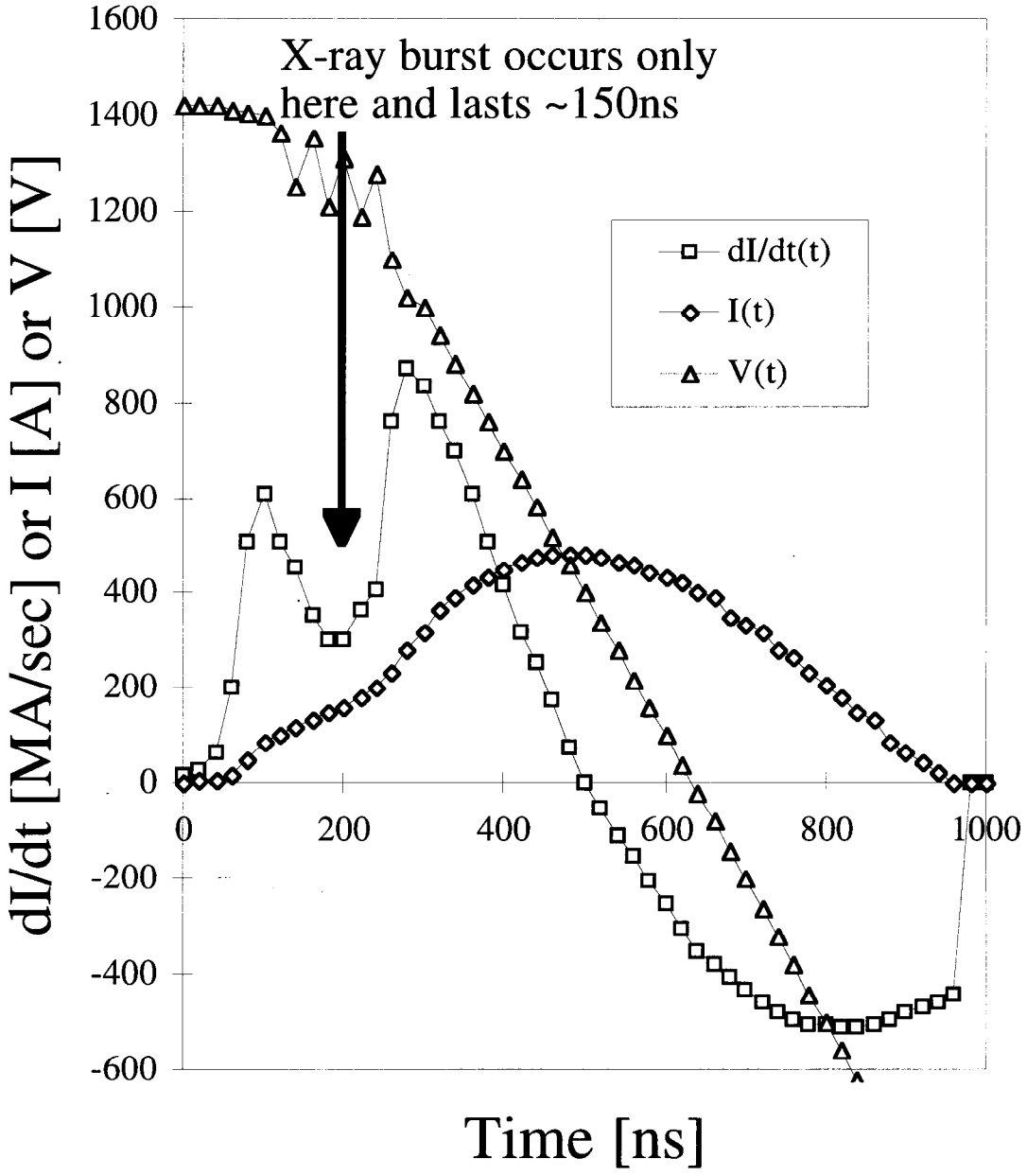
X-ray burst occurs only here and lasts ~150ns
dI/dt(t)
I(t)
V(t)
dI/dt [MA/sec] or I [A] or V [V]
Time [ns]
1600
1400
1200
1000
800
600
400
200
0
-200
-400
-600
0
200
400
600
800
1000

Fig. 14

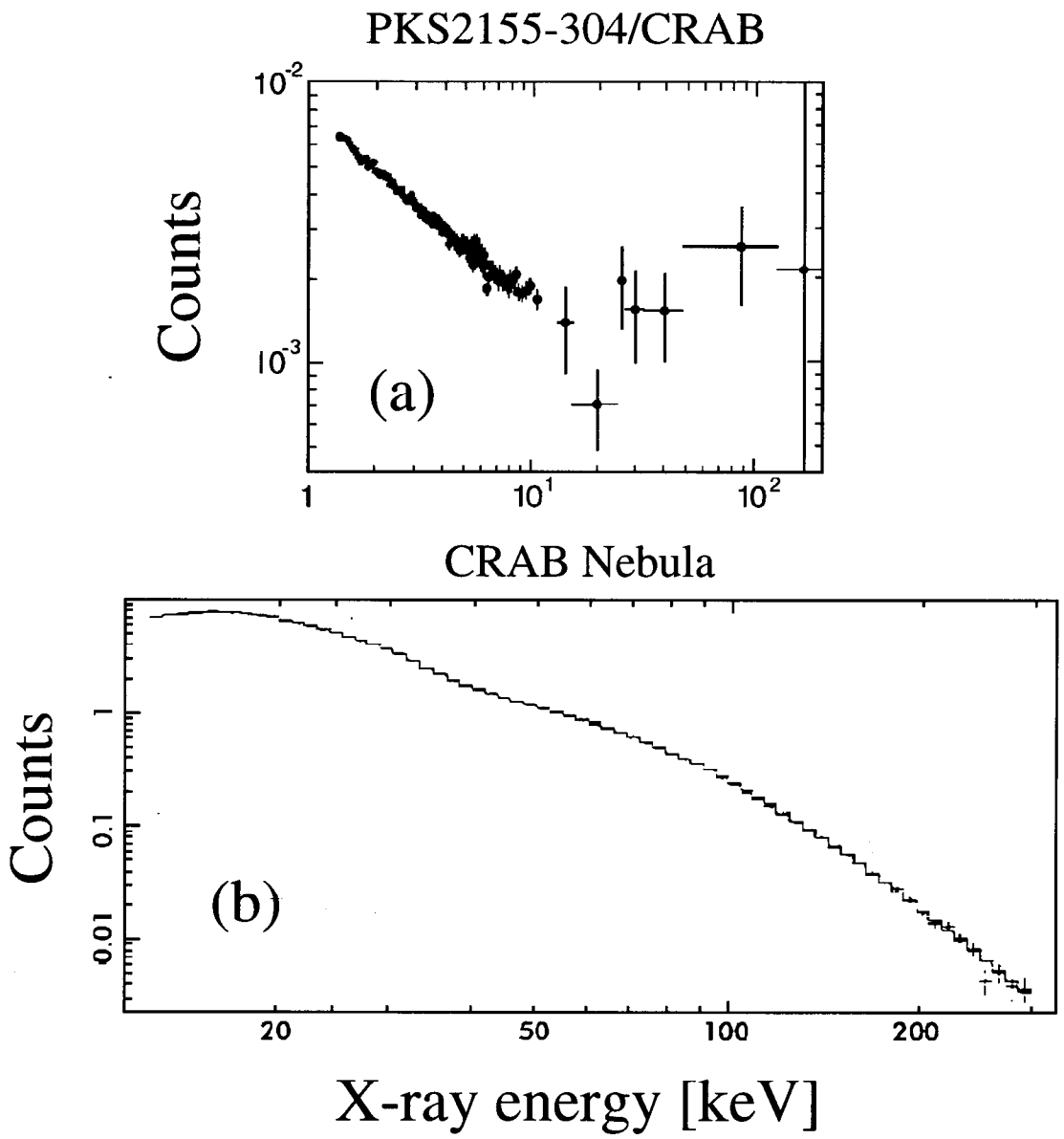
PKS2155-304/CRAB
Counts
10^{-2}
10^{-3}
(a)
1
10^{1}
10^{2}
CRAB Nebula
Counts
1
0.1
0.01
(b)
20
50
100
200
X-ray energy [keV]

Fig. 15